Oxygen and Al–Mg isotopic constraints on cooling rate and age of partial melting of an Allende Type B CAI, Golfball

Noriyuki Kawasaki [a,*], Shoichi Itoh [b], Naoya Sakamoto [c], Steven B. Simon [d], Daiki Yamamoto [e] and Hisayoshi Yurimoto [a,c]

[a]*Department of Natural History Sciences, Hokkaido University, Sapporo 060-0810, Japan*

[b]*Department of Earth and Planetary Sciences, Kyoto University, Kyoto 606-8502, Japan*

[c]*Isotope Imaging Laboratory, Creative Research Institution, Hokkaido University, Sapporo 001-0021, Japan*

[d]*Institute of Meteoritics, University of New Mexico, Albuquerque, New Mexico 87131, USA*

[e]*Institute of Space and Astronautical Science, Japan Aerospace Exploration Agency, Sagamihara 252-5210, Japan.*

*Corresponding author. Email: kawasaki@ep.sci.hokudai.ac.jp

Keywords: Ca-Al-rich inclusions; partial melting; oxygen isotopes; Al–Mg systematics

ABSTRACT

Coarse-grained, igneous Ca-Al-rich inclusions (CAIs) in CV chondrites formed through multiple melting events. We conducted *in situ* O-isotope analysis and Al−Mg systematics by secondary ion mass spectrometry of relict and overgrown minerals from a partial melting event in an Allende Type B CAI, Golfball. Golfball has a Type B CAI bulk composition and a unique structure: a fassaite-rich mantle enclosing a melilite-rich core. Many of the blocky melilite crystals in the core have irregularly-shaped, Al-rich ($Åk_{5–15}$) cores enclosed in strongly zoned ($Åk_{30–70}$) overgrowths. Since the Al-rich melilite grains could not have formed from a melt of Golfball, they are interpreted as relict grains that survived later melting events. The O-isotopic compositions of the blocky melilite crystals plot along the carbonaceous chondrite anhydrous mineral line, ranging between $\Delta^{17}O \sim -14‰$ and −5‰. The Al-rich relict melilite grains and their overgrowths exhibit the same O-isotopic compositions, while the O-isotopic compositions are varied spatially among melilites. We found that the O-isotopic compositions steeply change across several melilite crystals within few tens of micrometers, indicating the O-isotopic compositions of the melt could not have been homogenized during the partial melting in that scale. According to the timescale of O self-diffusivity in the melt, the cooling rate of the partial melting event is calculated to be $> 6 \times 10^4$ K/h. Al−Mg isotope data for core minerals plot on a straight line on an Al−Mg evolution diagram. A mineral isochron for Golfball gives initial $^{26}Al/^{27}Al$ of $(4.42 \pm 0.20) \times 10^{-5}$ and initial $\delta^{26}Mg^*$ of $-0.035 \pm 0.050‰$. The chemical and O-isotopic compositions of melilite and those initial values imply that its precursor consisted of fluffy Type A and/or fine-grained CAIs. The partial melting event for Golfball may have occurred in very short order after the precursor formation.

1. INTRODUCTION

Ca-Al-rich inclusions (CAIs) in chondrites are the oldest objects formed in the Solar System (Connelly et al., 2012). Coarse-grained, compact Type A, Type B, and Type C CAIs in CV chondrites experienced melting and solidification and are thus igneous in origin (e.g., MacPherson and Grossman, 1981; Wark and Lovering, 1982; Wark, 1987; Simon et al., 1999). They exhibit unequilibrated O-isotopic compositions distributed along the carbonaceous chondrite anhydrous mineral (CCAM) line, a nearly slope-1 line on an O three-isotope diagram (Clayton et al., 1977; Clayton, 1993). Coarse-grained, igneous CAIs have been suggested to have experienced multiple melting events, based on their petrography and chemical and O-isotopic distributions (MacPherson and Davis, 1993; Yurimoto et al., 1998; Beckett et al., 2000; Ito et al., 2004; Simon et al., 2005; Yoshitake et al., 2005; Aléon et al., 2007; Krot et al., 2008a; Wakaki et al., 2013; Aléon, 2016; Kawasaki et al., 2015, 2018).

Most CAIs contained ^{26}Al, a short-lived radionuclide with a half-life of 0.705 Myr (Norris et al., 1983), at the time of their formation (e.g., Lee et al., 1976; MacPherson et al., 1995). The Al–Mg systematics of individual CAIs in CV chondrites revealed that coarse-grained, igneous CAIs and condensate CAIs, such as fluffy Type A (FTAs) and fine-grained CAIs (FGIs), exhibit similar variations in initial ^{26}Al/^{27}Al values, $(^{26}\mathrm{Al}/^{27}\mathrm{Al})_0$ (e.g., MacPherson et al., 2010, 2012, 2017; Kita et al., 2012; Kawasaki et al., 2019, 2020); the processes of condensation and melting for CAI formation occurred contemporaneously during the first ~0.4 Myr of the Solar System formation (Kawasaki et al., 2020). Formation events of Type C CAIs may be related to chondrule formation, and their inferred low $(^{26}\mathrm{Al}/^{27}\mathrm{Al})_0$ imply their last melting events occurred > ~2 Myr after formation of most CAIs (e.g., Krot et al., 2005, 2007; Kawasaki et al., 2015). However,

it is still debatable whether variations in $(^{26}Al/^{27}Al)_0$ among CAIs correspond to a formation age spread or heterogeneous distributions of ^{26}Al in the forming region (e.g., Wasserburg et al., 1977; Krot et al., 2008b; Jacobsen et al., 2008; Larsen et al., 2011, 2020; Makide et al., 2011; Holst et al., 2013; Kööp et al., 2016; Park et al., 2017; Kawasaki et al., 2019, 2020).

The Al−Mg systematics recorded by multiple partial melting events of individual igneous CAIs would constrain age differences between the melting and precursor formation events, regardless of the possibility of heterogeneous distributions of ^{26}Al. Internal, partial resetting of Al−Mg system of CAIs by partial melting has been suggested by several studies (Podosek et al., 1991; Hsu et al., 2000; MacPherson et al., 2012, 2018; Kawasaki et al., 2015). Ito et al. (2006) and Kawasaki et al. (2015) investigated the Al−Mg systematics of relict minerals and minerals that crystallized as a result of partial melting events, determined based on their petrography and O-isotope disequilibrium. The Al−Mg data for the relict melilite and later-crystallized melilite in an Allende compact Type A CAI 7R-19-1 do not show a resolvable age difference between them (Ito et al., 2006), although the analytical error of ~0.4 Myr is comparable to the inferred formation period of CV CAIs (Kawasaki et al., 2020). On the other hand, internal resetting of the Al−Mg system is demonstrated for an Allende Type C CAI, EK1-04-2, in which relict spinel grains and later-crystallized minerals from a partial melting event have a relative age difference of at least ~1.6 Myr (Kawasaki et al., 2015).

In this study, we determined the Al−Mg systematics of relict minerals and later-crystallized minerals from a partial melting event in an Allende Type B CAI, Golfball (Simon et al., 2005) by secondary ion mass spectrometry (SIMS). This CAI has a Type B CAI bulk composition (Simon and Grossman, 2004) and a unique structure of a thin

melilite mantle at the outermost edge, and a thicker fassaite-rich mantle enclosing a melilite-rich core (Fig. 1). It shows a clear signature of partial melting; Al-rich relict melilite grains (åkermanite contents in mol%, $Åk_{5–15}$) surrounded by strongly zoned overgrowths ($Åk_{30–70}$) are present in the core. In addition, we conducted *in situ* O-isotope analyses of the relict and overgrown melilites by SIMS. Based on disequilibrium distributions of O-isotopic compositions in melilite crystals, we constrain a cooling rate of the partial melting event. Preliminary results of O and Al−Mg isotope analyses of minerals in Golfball were reported by Itoh et al. (2009).

2. EXPERIMENTAL TECHNIQUES

2.1 Sample preparation and elemental analysis

The polished thin section of the Allende Type B CAI Golfball, section GBL2 (Simon et al., 2005), was coated with a carbon thin film (~20 nm) for backscattered electron (BSE) imaging, elemental analysis using an energy dispersive X-ray spectrometer (EDS), crystal orientation mapping using an electron backscatter diffraction (EBSD) system and O-isotope spot analysis by SIMS, and it was coated with a gold thin film (~70 nm) for O-isotope imaging and Al−Mg isotope analysis by SIMS.

BSE images were obtained using a field emission type scanning electron microscope (FE-SEM; JEOL JSM-7000F) at Hokkaido University. Quantitative X-ray elemental mapping was conducted using an EDS (Oxford X-Max 150) installed on the FE-SEM. A 15 keV electron beam probe with currents of 10 nA was employed. The åkermanite contents of O-isotope spot analysis locations in melilite were extracted from the quantitative åkermanite content map. Statistical error of the åkermanite contents of melilite extracted from an area of 2−3 μm, which corresponds to probe sizes of the SIMS

118 analysis, was less than 2 mol% (2σ). Grain boundaries of melilite crystals were
119 determined using an EBSD system (Oxford Aztec HKL) on the FE-SEM. A 20 keV
120 electron beam probe with currents of 4 nA was employed.

121 **2.2 Oxygen isotope spot analysis**

122 O-isotopic compositions for the minerals in Golfball were measured using a
123 SIMS instrument (Cameca ims-1280HR) of Hokkaido University, following the
124 analytical procedures reported in Kawasaki et al. (2018). A $^{133}Cs^{+}$ primary beam (20 keV,
125 ~30 pA) with a diameter of 2−3 μm was used. Negative secondary ions ($^{16}O^{-}$, $^{17}O^{-}$, and
126 $^{18}O^{-}$) were measured simultaneously in the multicollection mode. $^{16}O^{-}$, $^{17}O^{-}$, and $^{18}O^{-}$
127 were measured using a multicollector Faraday cup (10^{11} Ω, designed for L1), an axial
128 electron multiplier, and a multicollector electron multiplier (designed for H2),
129 respectively. A normal-incidence electron flood gun was used for electrostatic charge
130 compensation of the analyzing areas during the measurements. The mass resolution of
131 $M/\Delta M$ for $^{17}O^{-}$ was set at ~6000 to ensure that the contribution of $^{16}OH^{-}$ to $^{17}O^{-}$ is
132 negligible, while that for $^{16}O^{-}$ and $^{18}O^{-}$ was ~2000. The secondary ion intensity of $^{16}O^{-}$
133 was ~2 × 10^{7} cps. Each measurement was conducted with 30 cycles of counting the
134 secondary ions for 4 s. Obtained count rates were corrected for FC background, EM
135 deadtime, and relative yield of each detector. Synthetic gehlenite ($\delta^{18}O$ = 7.4‰) and
136 Russian spinel ($\delta^{18}O$ = 8.5‰) (Yurimoto et al., 1994) were used as standards to correct
137 instrumental mass fractionation for the CAI melilite and spinel, respectively. Analytical
138 errors include an internal error of individual analysis and an uncertainty of the
139 instrumental mass fractionation (assigned as 2SE of repetitive analyses of the standards).
140 Typical errors for $\delta^{17}O$, $\delta^{18}O$, and $\Delta^{17}O$ were 2.2‰, 1.0‰, and 2.3‰ (2σ), respectively.

141 **2.3 Oxygen isotope imaging**

Quantitative O-isotope imaging was conducted using an isotope microscope system (Cameca ims-1270e7 with SCAPS) of Hokkaido University (Yurimoto et al., 2003), following the analytical and data reduction procedures reported in Park et al. (2012) and Matsuda et al. (2019). A $^{133}Cs^{+}$ primary beam (15 keV, ~2 nA) was uniformly irradiated onto the sample surface as an oval shape with a traverse diameter of ~70 μm. A normal-incidence electron flood gun was used for the electrostatic charge compensation of the analyzing area. The contrast aperture of 150 μm was used. The energy slit and exit slit widths were set to 50 μm and 750 μm, respectively. After the pre-sputtering, secondary ion images were acquired using the following sequences and acquisition times in the order of $^{27}Al^{16}O^{-}$ for 50 s, $^{16}O^{-}$ for 5 s, $^{18}O^{-}$ for 200 s, $^{16}O^{-}$ for 5 s, $^{18}O^{-}$ for 200 s, $^{16}O^{-}$ for 5 s, $^{18}O^{-}$ for 200 s, and $^{16}O^{-}$ for 5 s. The calculated $^{18}O^{-}/^{16}O^{-}$ secondary ion ratio image was converted to the SMOW scale by normalization using the data of O-isotope spot analysis (#612−615, #617 and #618).

2.4 Al−Mg isotope analysis in multicollection mode

Mg-isotopic compositions and $^{27}Al/^{24}Mg$ ratios of the minerals in Golfball were measured using the SIMS instrument (Cameca ims-1280HR) of Hokkaido University, following the analytical procedures reported in Kawasaki et al. (2019, 2020). An $^{16}O^{-}$ primary beam accelerated to 23 keV was employed in the experiment. We used both the peak-jumping mode and the multicollection mode, depending on the secondary ion intensities of Mg-isotopes from the minerals. For Mg-rich melilite ($^{27}Al/^{24}Mg < 7$) and spinel, the Mg-isotopes ($^{24}Mg^{+}$, $^{25}Mg^{+}$, and $^{26}Mg^{+}$) and $^{27}Al^{+}$ were measured simultaneously in the multicollection mode with four Faraday cups: $^{24}Mg^{+}$ for L2* (10^{11} Ω), $^{25}Mg^{+}$ for L1 (10^{11} Ω), $^{26}Mg^{+}$ for H1 (10^{11} Ω), and $^{27}Al^{+}$ for H2* (10^{10} Ω). The primary beam was set to 25−28 nA with an almost circular shape of ~19 μm for the Mg-rich

166 melilite measurements and ~6 nA with an elliptical shape of 7 × 11 μm for the spinel
167 measurements. The mass resolution of $M/\Delta M$ was set at ~2000. The contributions of ion
168 interferences (e.g., $^{48}Ca^{2+}$, $^{24}MgH^{+}$, $^{25}MgH^{+}$, and $^{52}Cr^{2+}$) were negligible under these
169 conditions. The secondary ion intensities of $^{24}Mg^{+}$ were 1.1−1.3 × 10^{8} and ~2.4 × 10^{8} cps
170 for Mg-rich melilite and spinel, respectively. Each measurement was conducted with 20
171 cycles of counting the secondary ions for 10 s. Obtained count rates were corrected for
172 FC background and relative yield of each detector. The relative sensitivity factors for Al
173 and Mg were determined through measurements of synthetic melilite glasses and Russian
174 spinel for melilite and spinel, respectively. The mass-dependent fractionations of Mg-
175 isotopes for the minerals in Golfball are reported as $\delta^{25}Mg_{DSM3}$ values (permil deviation
176 from Mg reference material DSM-3; Galy et al., 2003). The $\delta^{25}Mg_{DSM3}$ for the synthetic
177 melilite glasses is −1.76 ± 0.13‰ measured with multi-collector inductively coupled
178 plasma-mass spectrometry (MC-ICP-MS), and they are used for the corrections of
179 melilite in Golfball. The $\delta^{25}Mg_{DSM3}$ value for Russian spinel was assumed to be zero for
180 the correction of spinel in Golfball.
181 The excess of radiogenic ^{26}Mg, $\delta^{26}Mg^{*}$, was calculated via an exponential
182 fractionation law with coefficient $\alpha_{natural}$ = 0.5128 because natural fractionation for Mg-
183 isotopes is considered to be controlled by evaporation processes (Davis et al., 2015).
184 However, the natural mass fractionation deviates from the instrumental mass fractionation
185 of SIMS, and the instrumental mass fractionation also differs among target minerals and
186 among analytical sessions under the measurement conditions (Itoh et al., 2008; Kawasaki
187 et al., 2017, 2018, 2019, 2020). We determined instrumental mass fractionation, α_{SIMS},
188 through measurements of terrestrial standards to calculate the excess radiogenic ^{26}Mg in
189 each analytical session. The α_{SIMS} values for Mg-rich melilite and spinel were determined

via linear regressions of the Φ^{25}Mg and Φ^{26}Mg values of Takashima augite and each of the standard, the synthetic melilite glasses and Russian spinel, respectively, where $\Phi^{25,26}\mathrm{Mg} = 1000 \times \ln[(^{25,26}\mathrm{Mg}/^{24}\mathrm{Mg})_{\mathrm{sample}}/(^{25,26}\mathrm{Mg}/^{24}\mathrm{Mg})_{\mathrm{ref.}}]$. The terrestrial reference ratios of $(^{25}\mathrm{Mg}/^{24}\mathrm{Mg})_{\mathrm{ref.}} = 0.12663$ and $(^{26}\mathrm{Mg}/^{24}\mathrm{Mg})_{\mathrm{ref.}} = 0.13932$ (Catanzaro et al., 1966) were used for δ^{26}Mg* calculations, although the final corrected δ^{26}Mg* values are independent of the reference ratios used. In this study, the α_{SIMS} for Mg-rich melilite were found to be 0.498 ± 0.002 (2σ), 0.498 ± 0.003 and 0.501 ± 0.002 for different three sessions and the α_{SIMS} for spinel were 0.513 ± 0.002 and 0.516 ± 0.003 for different two sessions. From the results of the linear regressions, an instrumental offset for the δ^{26}Mg* values, β, which ranged from −0.50 to −0.54 with errors of 0.01−0.02 depending on minerals and analytical sessions, was identified. The fractionation-corrected δ^{26}Mg* values for CAI minerals were determined by the following equation

$$\delta^{26}\mathrm{Mg}^* = \delta^{26}\mathrm{Mg}_{\mathrm{sample}} - \left[\left(1 + \frac{\delta^{25}\mathrm{Mg}_{\mathrm{sample}}}{1000}\right)^{\frac{1}{\alpha_{natural}}} - 1\right] \times 1000$$
$$- \beta + \left[\left(1 + \frac{\delta^{25}\mathrm{Mg}_{\mathrm{std}}}{1000}\right)^{\frac{1}{\alpha_{natural}}} - 1\right] \times 1000$$
$$- \left[\left(1 + \frac{\delta^{25}\mathrm{Mg}_{\mathrm{std}}}{1000}\right)^{\frac{1}{\alpha_{SIMS}}} - 1\right] \times 1000,$$

where $\delta^{25,26}\mathrm{Mg}_{\mathrm{sample}} = [(^{25,26}\mathrm{Mg}/^{24}\mathrm{Mg})_{\mathrm{sample}}/(^{25,26}\mathrm{Mg}/^{24}\mathrm{Mg})_{\mathrm{ref.}} - 1] \times 1000$, $\delta^{25}\mathrm{Mg}_{\mathrm{std}} = [(^{25}\mathrm{Mg}/^{24}\mathrm{Mg})_{\mathrm{std}}/(^{25}\mathrm{Mg}/^{24}\mathrm{Mg})_{\mathrm{ref.}} - 1] \times 1000$. More details and the error estimation procedure are described elsewhere (Kawasaki et al., 2017). The analytical errors (2σ) for δ^{26}Mg* were ~0.13‰ for Mg-rich melilite and ~0.07‰ for spinel.

2.5 Al−Mg isotope analysis in peak-jumping mode

For Mg-poor melilite ($^{27}Al/^{24}Mg > 16$), Mg-isotopes ($^{24}Mg^+$, $^{25}Mg^+$, and $^{26}Mg^+$) were measured using an axial electron multiplier, while $^{27}Al^+$ was measured using a multicollector Faraday cup (10^{11} Ω, designed for H2*) simultaneously with $^{25}Mg^+$, in peak-jumping mode. An $^{16}O^-$ primary beam accelerated to 23 keV was employed in the experiment. The primary beam current was set to ~140 pA with an elliptical shape of 3 × 5 μm. The mass resolution of $M/\Delta M$ was set at ~4000, which is sufficient to resolve ion interferences (e.g., $^{48}Ca^{2+}$, $^{24}MgH^+$, $^{25}MgH^+$, and $^{52}Cr^{2+}$). The secondary ion intensities of $^{24}Mg^+$ were 0.1−1.5 × 10^5 cps. Each measurement was conducted for 100 cycles with a counting sequence with $^{24}Mg^+$ for 2 s, $^{25}Mg^+$ for 2 s, $^{25}Mg^+$ and $^{27}Al^+$ for 4 s, and $^{26}Mg^+$ for 6 s. The obtained count rates were corrected for the FC background and EM deadtime. The instrumental mass fractionation and relative sensitivity factor for Al and Mg were determined through measurements of synthetic melilite glasses. The calculation methods of $\delta^{26}Mg^*$ and $\delta^{25}Mg_{DSM3}$ are essentially identical to those described in Section 2.4 although α_{SIMS} and β were not determined in the peak-jumping mode because the instrumental mass fractionation and natural mass fractionation were indistinguishable from each other under the measurement conditions here. The analytical errors for $\delta^{26}Mg^*$ were assigned as internal errors (2SE) and were 1.1−1.7‰.

3. RESULTS

3.1 Mineralogy and petrology

Fig. 1 shows BSE and elemental maps of Golfball, section GBL2, which has a rounded shape with a diameter of ~7 mm. Detailed petrography and mineral chemistry of Golfball are presented in Simon et al. (2005). The bulk chemical composition of Golfball was determined by a modal recombination technique by Simon and Grossman (2004),

231 showing a Type B CAI bulk composition. Golfball has a core-mantle structure of a
232 melilite-rich core enclosed by a fassaite-rich mantle and a relatively thin outermost
233 melilite mantle, which has not been observed in other Type B CAIs. Some melilite laths
234 appear to have nucleated on the edge of the CAI and then grew inward (Simon et al.,
235 2005).

236 The melilite-rich core is mainly composed of blocky melilite crystals with sizes
237 typically 20−50 μm across (Fig. 2), plus several lathlike melilite crystals protruding from
238 the core into the mantle (Fig. 3a). The blocky melilite crystals enclose many small spinel
239 crystals and are separated by pockets of fassaite, spinel, and rare anorthite. Fassaite
240 crystals with sizes of ~1 mm across (Fig. 1d) poikilitically enclose the blocky melilite and
241 spinel crystals (Fig. 2a). The blocky melilite crystals are very strongly concentrically
242 zoned; they exhibit typically normal zoning from ~$Åk_{30}$ to ~$Åk_{70}$, but some have Mg-rich
243 cores (up to ~$Åk_{60}$) to form oscillatory zoning (Fig. 2). They also often contain irregularly
244 shaped Al-rich cores, typically ~$Åk_{5–15}$, enclosed in strongly zoned overgrowths
245 (typically ~$Åk_{30–70}$) (Figs. 2 and 4; Figs. 4 and 5 of Simon et al. 2005). The thin
246 transitional zones observed between the Al-rich grains and the overgrowths were reported
247 to be ~5 μm wide inferred from the electron microprobe traverse (Fig. 5 of Simon et al.
248 2005), but new data for many Al-rich grains, after the careful examination of X-ray
249 mapping in this study, indicate that the width of transitional zones is ~1 μm (e.g., Fig. 4d),
250 which is slightly larger than the spatial resolution of 0.6 μm estimated for the EDS line
251 profile from a boundary between spinel and melilite defined by the width between the
252 16% and 84% level. The wider transitional zones of the previous study may be due to
253 fluorescence effects of X-ray generation by slanting grain boundaries.

254 The fassaite-rich mantle is ~1 mm thick and mainly composed of fassaite and

spinel. The subhedral to nearly euhedral, mantle fassaite crystals poikilitically enclose abundant spinel crystals. Primary, anhedral anorthite crystals occur typically adjacent to the fassaite crystals. At the outer edge of the inclusion, radially oriented melilite laths occur (Figs. 1 and 3b; Fig. 1d of Simon et al. 2005). The lath melilite crystals in the rim are ~500 μm long and show inward growth zoning from ~$Åk_{30}$ to ~$Åk_{70}$, and then back to ~$Åk_{50}$, probably due to the onset of cocrystallization with fassaite (MacPherson et al., 1984).

3.2 O-isotopic compositions

The measured O-isotopic compositions of minerals in Golfball and locations of SIMS measurements are summarized in Supplementary materials. Fig. 5 shows the O-isotopic compositions plotted on the O three-isotope diagram. The O-isotopic compositions of minerals are distributed along the CCAM line within error. Compositions range between $\Delta^{17}O \sim -23‰$ and −5‰, which shows O-isotope disequilibrium in the CAI.

The spinel in the core exhibits homogeneously ^{16}O-rich compositions ($\Delta^{17}O = -24.0 \pm 1.9‰$, 2SD), despite their different petrographic settings (Table 1). On the other hand, O-isotopic compositions of the blocky melilite crystals in the core exhibit significant variations, ranging from $\Delta^{17}O \sim -14$ to −5‰ (Fig. 5).

The O-isotopic compositions of blocky melilite crystals in various areas are shown in Fig. 6. The O-isotopic compositions are not correlated with åkermanite contents (i.e., crystal growth), but show various distributions in each area. The melilites in the areas 1 to 3 exhibit compact $\Delta^{17}O$ distributions, but the average $\Delta^{17}O$ for area 3 ($\Delta^{17}O = -6.4 \pm 2.1‰$) is slightly ^{16}O-poorer than those for areas 1 (−9.0 ± 2.0‰) and 2 (−9.4 ± 2.0‰). There are no resolvable differences in O-isotopic compositions between the Al-

rich cores and the overgrowths in each area. The quantitative $\delta^{18}O$ image of a blocky melilite crystal containing Al-rich grain (Fig. 4f) clearly shows that O-isotopic composition is homogeneous within the whole crystal, supporting the characteristics shown in Figs. 6a to 6f. In area 4, the O-isotopic compositions of Al-rich grains are also identical to those of the most overgrown grains ($\Delta^{17}O \sim -8‰$), while the average $\Delta^{17}O$ is intermediate among those of the areas 1 to 3. Moreover, some overgrowths are slightly enriched in ^{16}O ($\Delta^{17}O \sim -10‰$). The O-isotopic compositions of melilite in area 5 show significant variations, ranging from $\Delta^{17}O \sim -14$ to $-8‰$. Fig. 7 shows the O-isotopic compositions ($\delta^{18}O$) of melilite grains in area 5. The O-isotopic compositions are not randomly distributed among measurement sites, but instead show long range patterns across numerous grains.

3.3 Al-Mg isotopic compositions

The Mg-isotopic compositions and $^{27}Al/^{24}Mg$ ratios measured for minerals in Golfball are summarized in Table 2. Fig. 8 shows the Mg-isotopic compositions and $^{27}Al/^{24}Mg$ ratios of minerals in the core of Golfball plotted on the ^{26}Al–^{26}Mg evolution diagrams. The Al−Mg isotope data perfectly plot on a straight line. If we define an ^{26}Al–^{26}Mg mineral isochron, the isochron gives initial values of $(^{26}Al/^{27}Al)_0 = (4.42 \pm 0.20) \times 10^{-5}$ and initial $\delta^{26}Mg^*$, $(\delta^{26}Mg^*)_0 = -0.035 \pm 0.050‰$.

Averages of $\delta^{25}Mg_{DSM3}$ values for Al-rich melilite grains, overgrown melilite grains, and spinel are $1.4 \pm 1.5‰$ (2SD, $n = 12$), $1.8 \pm 0.2‰$ ($n = 3$) and $1.79 \pm 0.13‰$ ($n = 6$), respectively. These $\delta^{25}Mg_{DSM3}$ values by SIMS are consistent with the bulk Mg-isotopic composition for Golfball, $\delta^{25}Mg_{DSM3} = 1.61 \pm 0.06‰$ (Grossman et al., 2008), measured by MC-ICP-MS.

303 # 4. DISCUSSION

304 ## 4.1 Cooling rate of partial melting event inferred from O-isotopic distributions

305 As discussed in Simon et al. (2005), the Al-rich grains in blocky melilite crystals
306 in Golfball could not have crystallized from a liquid having chemical composition of bulk
307 Golfball or even that of its core (Simon and Grossman, 2004), according to the inferred
308 initial melilite compositions crystallized from a CMAS melt (Beckett et al., 1999). Thus,
309 they are relict grains that survived partial melting events (see also Fig. 11 of Simon et al.
310 2005). The Al-rich relict grains and the surrounding overgrown melilite grains in areas 1
311 to 3 have the same O-isotopic composition as each other (Figs. 4f, 6a, 6c and 6e),
312 indicating O-isotopes of the overgrown melilite grains are inherited from those of
313 precursor materials. Moreover, the O-isotopic compositions of melilite exhibit spatial
314 variations as observed in areas 4 and 5 (Figs. 6g, 6i and 7). Because the O-isotopic
315 compositions of melilite crystals are not correlated with their åkermanite contents (i.e.,
316 crystal growth) (Fig. 6), the O-isotopic variations cannot be attributed to a temporal
317 change of O-isotopic composition of the melt during cooling after the partial melting
318 events.

319 Fig. 9 shows O-isotopic compositions along a linear traverse across melilite
320 crystals in area 5 (Fig. 7). The O-isotopic compositions of melilite crystals steadily change
321 within a zone of ~21 μm width while the first 40 μm and the last 40 μm of the traverse
322 exhibit almost flat distributions of O-isotopic compositions, with $\delta^{18}O \sim -20‰$ and $\delta^{18}O$
323 $\sim -12‰$, respectively. Because those flat distributions could be inheritance of the O-
324 isotopic variations of precursor materials having $\delta^{18}O$ of $\sim -20‰$ and $\sim -12‰$, the
325 monotonic change zone could have been formed by O-isotope diffusion in the melt during
326 partial melting. The diffusion distance ($(Dt)^{1/2}$, D: diffusion coefficient, t: time) of O-

isotope in the melt can be determined to be ~11 μm, using a diffusion model with the initial condition of two semi-infinite sources (Shewmon, 1963). The heterogeneity of O-isotopic compositions strongly suggests that O-isotope exchange between the melt and surrounding nebular gas, as suggested for many coarse-grained CAIs (e.g., Yurimoto et al., 1998; Kawasaki et al., 2018), did not occur during crystallization of these melilites in Golfball. The lack of the gas-melt O-isotope exchange was also suggested for other CAIs (Aléon, 2016, 2018).

To preserve the O-isotope gradient in the melt inherited from precursor materials during the partial melting event, melilite crystallization accompanied by cooling must have been completed prior to homogenization of O-isotopes. A cooling rate after the heating that caused the partial melting event can be estimated from the diffusion distance, applying a non-isothermal diffusion model (Lasaga, 1983) and the inferred maximum temperature, ~1400°C, of the early partial melting event (step 1 of Fig. 11 of Simon et al. 2005). Using an O self-diffusion coefficient of 1.62×10^{-7} cm^2 sec^{-1} at 1420°C for a CAIB melt (Yamamoto et al., 2019) and an activation energy of 170 kJ/mol for O self-diffusion in dry basaltic liquid (Lesher et al., 1996), a cooling rate for the O self-diffusion distance of 11 μm is estimated to be 6×10^4 K/h. The cooling rate could be faster than 6×10^4 K/h if the original O-isotopic variations of precursor materials contribute to the observed O-isotope gradient. Such gradual O-isotopic compositions have been observed in melilite crystals of Type A CAIs (Katayama et al., 2012; Kawasaki et al., 2012; Park et al., 2012). In addition, if the solid-state diffusion of O-isotopes occurred during the later partial melting event and thermal metamorphism on the parent body, the O self-diffusion distance in the melt would be shorter than 11 μm. If this is the case, then the cooling rate could be faster than 6×10^4 K/h.

The estimated cooling rate of > 6×10^4 K/h is much faster than those inferred for CAIs, ~0.5−50 K/h from experimental studies (MacPherson et al., 1984; Stolper and Paque, 1986) and < ~1 K/h from a natural CAI (Kawasaki et al., 2018). That is even faster than those for chondrules from experimental studies (~1−3000 K/h: Jones et al., 2018 and references therein) but slower than those inferred from a natural chondrule (10^5−10^6 K/h: Yurimoto and Wasson, 2002). Although Golfball has a Type B CAI bulk composition, its mineral textures are quite unlike other Type B CAIs. Therefore, the cooling rates inferred for other CAIs may not be applied to this early heating event, in which the Golfball precursors were partially melted. A later heating event, after Na had been introduced into the inclusion (Simon et al., 2005), gave rise to Na-bearing, reversely zoned melilite, indicating a much slower cooling rate (MacPherson et al., 1984). The sharply contrasting inferred cooling rates for the two events that affected Golfball suggest that the formation of CAIs did not occur by a unique heating mechanism but by multiple heating mechanisms in the early Solar System.

4.2 Short time interval between precursor formation and partial melting event

During the first partial melting event, spinel was also the liquidus phase. Nevertheless, all the Al−Mg isotope data, which include both the relict and overgrowth minerals, plot on a well-defined, single isochron with $(^{26}Al/^{27}Al)_0 = (4.42 \pm 0.20) \times 10^{-5}$ and $(\delta^{26}Mg^*)_0 = -0.035 \pm 0.050$‰ (Fig. 8). The Al−Mg system of the Al-rich relict grains might have been reset during the partial melting event by Mg self-diffusion associated with Mg-isotope exchange with the melt, resulting in the single isochron. According to the timescale required to keep the O-isotope gradient in the melt discussed above, a diffusion distance of Mg-isotopes in the Al-rich melilite grains during the partial melting is calculated to be less than 0.03 μm, using Mg self-diffusion coefficients in gehlenite (Ito

and Ganguly, 2009). Furthermore, the transition zones show steep gradients of åkermanite contents over ~1 μm (Figs. 4c and 4d). Therefore, the interdiffusion distances of Al + Al vs. Mg + Si during the partial melting should be less than 1 μm if it occurred. At the temperatures between 1230 and 1400°C, interdiffusion coefficients of Al + Al vs. Mg + Si for gehlenitic melilite (Nagasawa et al., 2001) and the Mg self-diffusion coefficients for gehlenite are comparable to each other. Thus, the Mg self-diffusion distance in the Al-rich relict grains during the partial melting event should be less than ~1 μm, which is much smaller than the sizes of Al-rich relict grains. These two independent estimations of Mg-isotope mobility indicate that the Al−Mg system of the Al-rich relict grains have effectively been kept in a closed system during the partial melting event. The well-defined mineral isochron suggests that the partial melting event occurred in very short order after precursor formation. Based on analytical errors of $(^{26}Al/^{27}Al)_0$, the time gap between the precursor formation and the partial melting event is shorter than 0.09 Myr.

4.3 Precursor of Golfball

If Al/Mg chemical fractionation for Golfball occurred at the formation time of "canonical" CAIs with $(^{26}Al/^{27}Al)_0 = \sim 5.2 \times 10^{-5}$ (Jacobsen et al., 2008; Larsen et al., 2011), the Mg-isotopic composition of Golfball would have evolved with the bulk $^{27}Al/^{24}Mg$ of 2.4 (Simon and Grossman, 2004) on an evolution curve shown as the green-colored area in the Mg-isotope evolution diagram of Fig. 10, to have $(\delta^{26}Mg^*)_0 = 0.10 \pm 0.05‰$ at $^{26}Al/^{27}Al = (4.42 \pm 0.20) \times 10^{-5}$. However, the inferred $(\delta^{26}Mg^*)_0$ of $-0.035 \pm 0.050‰$ is clearly lower than that evolved value, suggesting Golfball is not an object formed by remelting of canonical CAIs formed when $^{26}Al/^{27}Al = \sim 5.2 \times 10^{-5}$.

Instead, on the Mg-isotope evolution diagram (Fig. 10), the initial values of Golfball plot on the Mg-isotope evolution curve of solar-composition gas. Initial values,

399 $(^{26}Al/^{27}Al)_0$ and $(\delta^{26}Mg^*)_0$, for FTAs and FGIs also all plot on the Mg-isotope evolution
400 curve of solar-composition gas, despite their significant variations in $(^{26}Al/^{27}Al)_0$ from
401 ~5.2 to ~3.4×10^{-5} (Fig. 10). This consistency of initial values for Golfball with those for
402 the FTAs and FGIs implies that precursor materials of Golfball contained FTAs and/or
403 FGIs. The presence of Al-rich melilite with <$Åk_{15}$ is very common in FTAs and FGIs
404 from the CV chondrites (e.g., MacPherson and Grossman, 1984; Katayama et al., 2012;
405 Kawasaki et al., 2020; Wada et al., 2020) and O-isotopic compositions of their melilite
406 crystals have been reported to exhibit disequilibrium distributions along the CCAM line
407 between $\Delta^{17}O \sim -23‰$ and 1‰ (e.g., Katayama et al., 2012; Kawasaki et al., 2012, Wada
408 et al., 2020), which covers the range of O-isotopic variations ($\Delta^{17}O \sim -14‰$ to −5‰)
409 observed for the blocky melilite crystals in the Golfball core. This consistency of O-
410 isotopic compositions supports the above conclusion that the O-isotopic variations of the
411 blocky melilite crystals indicate inheritance of the O-isotope heterogeneity of precursor
412 materials. Furthermore, the $\delta^{25}Mg$ values of Al-rich relict melilite grains, averaging 1.4 ±
413 1.5‰, are consistent with ranges of those for melilite in FTAs (MacPherson et al., 2012;
414 Kawasaki et al., 2017, 2019) and FGIs (MacPherson et al., 2010; Kawasaki et al., 2020).
415 These chemical and O and Mg-isotopic signatures all suggest that the precursor of
416 Golfball contained FTAs and/or FGIs. The partial melting events affecting Golfball may
417 have occurred in very short order after the formation of precursor FTAs and/or FGIs.
418 The formation event of Golfball occurred at 0.18 ± 0.05 Myr after the formation
419 of canonical CAIs (Jacobsen et al., 2008; Larsen et al., 2011), under the assumption of
420 homogeneous distributions of ^{26}Al in the forming region. The remelting of Golfball CAI
421 is consistent with the conclusion that CAI-formation thermal processes of condensation
422 and melting occurred contemporaneously during ~0.4 Myr at the very beginning of the

Solar System (Kawasaki et al., 2020).

5. CONCLUSIONS

In situ O-isotope analysis and Al−Mg systematics of the Allende Type B CAI Golfball provide constraints on the cooling rate, age, and precursor materials of the CAI. Many of the blocky melilite crystals in the core of Golfball contain Al-rich relict grains that are enclosed in strongly zoned overgrowths. The O-isotopic compositions of the blocky melilite crystals range between $\Delta^{17}O \sim -14‰$ and $-5‰$. The Al-rich relict melilite grains and their overgrowths exhibit the same O-isotopic compositions, while the O-isotopic compositions are varied spatially among melilites. We found an area in which O-isotopic compositions gradually change across several melilite crystals over a distance of ~21 μm. The O-isotopic compositions of the melt could not have been homogenized during the partial melting event in that scale and thus O-isotope exchange with the nebular gas was insufficient in the Golfball melt if it occurred. Using the O self-diffusion coefficient in the melt, a cooling rate following partial melting is calculated to be 6×10^4 K/h or more. The Golfball experienced an extremely short heating event, differing from heating of typical Type B CAIs. The Al−Mg isotope data, including the relict and overgrown minerals, plot on the well-defined single mineral isochron with initial values of $(^{26}Al/^{27}Al)_0 = (4.42 \pm 0.20) \times 10^{-5}$ and $(\delta^{26}Mg^*)_0 = -0.035 \pm 0.050‰$. The consistency of the initial values and chemical and O-isotopic compositions of melilite with those for FTAs and FGIs implies that precursor materials of Golfball contained FTAs and/or FGIs. The partial melting events for Golfball may have occurred in very short order after the formation of precursor FTAs and/or FGIs, supporting the contemporaneous formation of condensate CAIs and igneous CAIs.

ACKNOWLEDGMENTS

This article is dedicated to Prof. John T. Wasson in honor of his outstanding contributions to cosmochemistry. We thank Andrew M. Davis and an anonymous reviewer for their constructive comments and the Associate Editor Yves Marrocchi for his editorial efforts. We thank Kosuke Nagata for technical assistance. This work is partly supported by Monka-sho grants.

REFERENCES

Aléon J., El Goresy A. and Zinner E. (2007) Oxygen isotope heterogeneities in the earliest protosolar gas recorded in a meteoritic calcium–aluminum-rich inclusion. *Earth and Planetary Science Letters* **263**, 114–127.

Aléon J. (2016) Oxygen isotopes in the early protoplanetary disk inferred from pyroxene in a classical type B CAI. *Earth and Planetary Science Letters* **440**, 62–70.

Aléon J. (2018) Closed system oxygen isotope redistribution in igneous CAIs upon spinel dissolution. *Earth and Planetary Science Letters* **482**, 324–333.

Beckett J. R., Paque J. M. and Stolper E. (1999) The use of melilite compositions to constrain the thermal history and liquid line of descent of type B CAIs. *Lunar Planetary Science Conference* **30**, #1920.

Beckett J. R., Simon S. B. and Stolper E. (2000) The partitioning of Na between melilite and liquid: Part II. Applications to Type B inclusions from carbonaceous chondrites. *Geochimica et Cosmochimica Acta* **64**, 2519–2534.

469 Catanzaro, E. J., Murphy, T. J., Garner, E. L. and Shields, W. R. (1966) Absolute isotopic
470 abundance ratios and atomic weights of magnesium. *J. Res. natl. Bur Stand.* **70a**,
471 453-458.
472 Clayton R. N., Onuma N., Grossman L. and Mayeda T. K. (1977) Distribution of the
473 presolar component in Allende and other carbonaceous chondrites. *Earth and*
474 *Planetary Science Letters* **34**, 209–224.
475 Clayton R. N. (1993) Oxygen isotopes in meteorites. *Annual Review of Earth and*
476 *Planetary Sciences* **21**, 115–149.
477 Connelly J. N., Bizzarro M., Krot A. N., Nordlund Å., Wielandt D. and Ivanova M. A.
478 (2012) The absolute chronology and thermal processing of solids in the solar
479 protoplanetary disk. *Science* **338**, 651–655.
480 Galy A., Yoffe O., Janney P. E., Williams R. W., Cloquet C., Alard O., Halicz L., Wadhwa
481 M., Hutcheon I. D., Ramon E. and Carignan J. (2003) Magnesium isotope
482 heterogeneity of the isotopic standard SRM980 and new reference materials for
483 magnesium-isotope-ratio measurements. *Journal of Analytical Atomic*
484 *Spectrometry*. **18**, 1352–1356.
485 Grossman L., Simon S. B., Rai V. K., Thiemens M. H., Hutcheon I. D., Williams R. W.,
486 Galy A., Ding T., Fedkin A. V., Clayton R. N. and Mayeda T. K. (2008) Primordial
487 compositions of refractory inclusions. *Geochimica et Cosmochimica Acta* **72**,
488 3001–3021.
489 Davis A. M., Richter F. M., Mendybaev R. A., Janney P. E., Wadhwa M. and McKeegan
490 K. D. (2015) Isotopic mass fractionation laws for magnesium and their effects on
491 ^{26}Al–^{26}Mg systematics in solar system materials. *Geochimica et Cosmochimica*
492 *Acta* **158**, 245–261.

493 Holst J. C., Olsen M. B., Paton C., Nagashima K., Schiller M., Wielandt D., Larsen K. K.,
494 Connelly J. N., Jorgensen J. K., Krot A. N., Nordlund A. and Bizzarro M. (2013)
495 ^{182}Hf-^{182}W age dating of a ^{26}Al-poor inclusion and implications for the origin of
496 short-lived radioisotopes in the early Solar System. *Proceedings of the National*
497 *Academy of Sciences of the United States of America* **110**, 8819–8823.
498 Hsu W., Wasserburg G. J. and Huss G. R. (2000). High time resolution by use of the ^{26}Al
499 chronometer in the multistage formation of a CAI. *Earth and Planetary Science*
500 *Letters* **182**, 15–29.
501 Ito, M., Nagasawa, H. and Yurimoto, H. (2004) Oxygen isotopic SIMS analysis in Allende
502 CAI: details of the very early thermal history of the solar system. *Geochimica et*
503 *Cosmochimica Acta* **68**, 2905–2923.
504 Ito M., Nagasawa H. and Yurimoto H. (2006) A study of Mg and K isotopes in Allende
505 CAIs: Implications to the time scale for the multiple heating processes.
506 *Meteoritics & Planetary Science* **41**, 1871–1881.
507 Ito M. and Ganguly J. (2009) Magnesium diffusion in minerals in CAIs: new
508 experimental data for melilites and implications for the Al-Mg chronometer and
509 thermal history of CAIs. *Lunar Planetary Science Conference* **40**, #1753.
510 Itoh S., Makide K. and Yurimoto H. (2008) Calculation of radiogenic ^{26}Mg of CAI
511 minerals under high precision isotope measurement by SIMS. *Applied Surface*
512 *Science* **255**, 1476–1478.
513 Itoh S., Simon S. B., Grossman L. and Yurimoto H. (2009) Al-Mg isochron study
514 combined with oxygen isotope analysis of the Allende type B CAI, Golfball.
515 (abstract #5307) 72nd Annual Meteoritical Society Meeting.
516 Jacobsen B., Yin Q., Moynier F., Amelin Y., Krot A. N., Nagashima K., Hutcheon I. D.

517 and Palme H. (2008) ^{26}Al-^{26}Mg and ^{207}Pb-^{206}Pb systematics of Allende CAIs:
518 Canonical solar initial ^{26}Al/^{27}Al ratio reinstated. *Earth and Planetary Science*
519 *Letters* **272**, 353–364.
520 Jones R. H., Villeneuve J. and Libourel G. (2018) Thermal histories of chondrules:
521 Petrologic observations and experimental constraints. In *Chondrules: Records of*
522 *Protoplanetary Disk Processes* (ed. S. S. Russel, H. C. Connolly Jr. and A. N.
523 Krot), pp. 57–90. Cambridge University Press.
524 Katayama J., Itoh S. and Yurimoto H. (2012) Oxygen isotopic zoning of reversely zoned
525 melilite crystals in a Fluffy Type A Ca-Al-rich inclusion from the Vigarano
526 meteorite. *Meteoritics & Planetary Science* **47**, 2094–2106.
527 Kawasaki N., Sakamoto N. and Yurimoto H. (2012) Oxygen isotopic and chemical zoning
528 of melilite crystals in a Type A Ca-Al-rich inclusion of Efremovka CV3 chondrite.
529 *Meteoritics & Planetary Science* **47**, 2084–2093.
530 Kawasaki, N., Kato, C., Itoh, S., Wakaki, S., Ito, M. and Yurimoto, H. (2015) ^{26}Al–^{26}Mg
531 chronology and oxygen isotope distributions of multiple melting for a Type C CAI
532 from Allende. *Geochimica et Cosmochimica Acta* **169**, 99–114.
533 Kawasaki N., Itoh S., Sakamoto N. and Yurimoto H. (2017) Chronological study of
534 oxygen isotope composition for the solar protoplanetary disk recorded in a fluffy
535 Type A CAI from Vigarano. *Geochimica et Cosmochimica Acta* **201**, 83–102.
536 Kawasaki N., Simon S. B., Grossman L., Sakamoto N. and Yurimoto H. (2018) Crystal
537 growth and disequilibrium distribution of oxygen isotopes in an igneous Ca-Al-
538 rich inclusion from the Allende carbonaceous chondrite. *Geochimica et*
539 *Cosmochimica Acta* **221**, 318–341.
540 Kawasaki N., Park C., Sakamoto N., Park S. Y., Kim H. N., Kuroda M. and Yurimoto H.

(2019) Variations in initial $^{26}Al/^{27}Al$ ratios among fluffy Type A Ca–Al-rich inclusions from reduced CV chondrites. *Earth and Planetary Science Letters* **511**, 25–35.

Kawasaki N., Wada S., Park C., Sakamoto N. and Yurimoto H. (2020) Variations in initial $^{26}Al/^{27}Al$ ratios among fine-grained Ca-Al-rich inclusions from reduced CV chondrites. *Geochimica et Cosmochimica Acta* **279**, 1–15.

Kita N. T., Ushikubo T., Knight K. B., Mendybaev R. A., Davis A. M., Richter F. M. and Fournelle J. H. (2012) Internal ^{26}Al-^{26}Mg isotope systematics of a Type B CAI: Remelting of refractory precursor solids. *Geochimica et Cosmochimica Acta* **86**, 37–51.

Kööp L., Davis A. M., Nakashima D., Park C., Krot A. N., Nagashima K., Tenner T. J., Heck P. R. and Kita N. T. (2016) A link between oxygen, calcium and titanium isotopes in ^{26}Al-poor hibonite-rich CAIs from Murchison and implications for the heterogeneity of dust reservoirs in the solar nebula. *Geochimica et Cosmochimica Acta* **189**, 70–95.

Krot A. N., Yurimoto H., Hutcheon I. D. and MacPherson G. J. (2005) Chronology of the early Solar System from chondrule-bearing calcium-aluminium-rich inclusions. *Nature* **434**, 998−1001.

Krot A. N., Yurimoto H., Hutcheon I. D., Chaussidon M., MacPherson G. J. and Paque J. (2007) Remelting of refractory inclusions in the chondrule-forming regions: Evidence from chondrule-bearing type C calcium-aluminum-rich inclusions from Allende. *Meteoritics & Planetary Science* **42**, 1197−1219.

Krot A. N., Chaussidon M., Yurimoto H., Sakamoto N., Nagashima K., Hutcheon I. D. and MacPherson G. J. (2008a) Oxygen isotopic compositions of Allende Type C

565 CAIs: Evidence for isotopic exchange during nebular melting and asteroidal
566 metamorphism. *Geochimica et Cosmochimica Acta* **72**, 2534–2555.
567 Krot A. N., Nagashima K., Bizzarro M., Huss G. R., Davis A. M., McKeegan K. D.,
568 Meyer B. S. and Ulyanov A. A. (2008b) Multiple generations of refractory
569 inclusions in the metal-rich carbonaceous chondrites Acfer 182/214 and Isheyevo.
570 *The Astrophysical Journal* **672**, 713–721.
571 Larsen K. K., Trinquier A., Paton C., Schiller M., Wielandt D., Ivanova M. A., Connelly
572 J. N., Nordlund Å., Krot A. N. and Bizzarro M. (2011) Evidence for magnesium
573 isotope heterogeneity in the solar protoplanetary disk. *The Astrophysical Journal*
574 *Letters* **735**, L37–L43.
575 Larsen K. K., Wielandt D., Schiller M., Krot A. N. and Bizzarro M. (2020) Episodic
576 formation of refractory inclusions in the Solar System and their presolar heritage.
577 *Earth and Planetary Science Letters* **535**, 116088.
578 Lasaga A. C. (1983) Geospeedometry: an extension of geothermometry. In Kinetics and
579 Equilibrium in Mineral Reactions (ed. S. K. Saxena), pp. 81–114, Springer-Varlag,
580 New York.
581 Lesher C. E., Hervig R. L. and Tinker D. (1996) Self diffusion of network formers (silicon
582 and oxygen) in naturally occurring basaltic liquid. *Geochimica et Cosmochimica*
583 *Acta* **60**, 405–413.
584 Lee T., Papanastassiou D. A. and Wasserburg G. J. (1976) Demonstration of ^{26}Mg excess
585 in Allende and evidence for ^{26}Al. *Geophysical Research Letters* **3**, 41–44.
586 Lodders K. (2003) Solar system abundances and condensation temperatures of the
587 elements. *The Astrophysical Journal* **591**, 1220–1247.
588 Ludwig K. (2003) ISOPLOT: A Geochronological Toolkit for Microsoft Excel 3.00.

589 Berkeley Geochronological Center Special Publication No. 4, Berkeley, CA 94709.
590 MacPherson G. J. and Grossman L. (1981) A once-molten, coarse-grained, Ca-rich
591 inclusion in Allende. *Earth and Planetary Science Letters* **52**, 16–24.
592 MacPherson G. J. and Grossman L. (1984) Fluffy Type A Ca-, Al-rich inclusions in the
593 Allende meteorite. *Geochimica et Cosmochimica Acta* **48**, 29−46.
594 MacPherson G. J., Paque J. M., Stolper E. and Grossman L. (1984) The origin and
595 significance of reverse zoning in melilite from Allende Type B inclusions. *The*
596 *Journal of Geology* **92**, 289–305.
597 MacPherson G. J. and Davis A. M (1993) A petrologic and ion microprobe study of a
598 Vigarano Type B refractory inclusions: Evolution by multiple stages of alteration
599 and melting. *Geochimica et Cosmochimica Acta* **57**, 231–243.
600 MacPherson G. J., Davis A. M. and Zinner E. K. (1995) The distribution of aluminum-26
601 in the early Solar System-A reappraisal. *Meteoritics* **30**, 365–386.
602 MacPherson G. J., Bullock E. S., Janney P. E., Kita N. T., Ushikubo T., Davis A. M.,
603 Wadhwa M. and Krot A. N. (2010) Early solar nebular condensates with canonical,
604 not supracanonical, initial $^{26}Al/^{27}Al$ ratios. *The Astrophysical Journal Letters* **711**,
605 L117–L121.
606 MacPherson G. J., Kita N. T., Ushikubo T., Bullock E. S. and Davis A. M. (2012) Well-
607 resolved variations in the formation ages for Ca-Al-rich inclusions in the early
608 Solar System. *Earth and Planetary Science Letters* **331**–**332**, 43–54.
609 MacPherson G. J., Bullock E. S., Tenner T. J., Nakashima D., Kita N. T., Ivanova M. A.,
610 Krot A. N., Petaev M. I. and Jacobsen S. B. (2017) High precision Al–Mg
611 systematics of forsterite-bearing Type B CAIs from CV3 chondrites. *Geochimica*
612 *et Cosmochimica Acta* **201**, 65–82.

MacPherson G. J., Defouilloy C. and Kita N. T. (2018) High-precision Al–Mg isotopic systematics in USNM 3898 – The benchmark "ALL" for initial $^{87}Sr/^{86}Sr$ in the earliest Solar System. *Earth and Planetary Science Letters* **491**, 238-243.

Makide K., Nagashima K., Krot A. N., Huss G. R., Ciesla F. J., Hellebrand E., Gaidos E. and Yang L. (2011) Heterogeneous distribution of ^{26}Al at the birth of the solar system. *The Astrophysical Journal Letters* **733**, L31–L34.

Matsuda N., Sakamoto N., Tachibana S. and Yurimoto H. (2019) Heating duration of igneous rim formation on a chondrule in the Northwest Africa 3118 $CV3_{oxA}$ carbonaceous chondrite inferred from micro-scale migration of the oxygen isotopes. *Geochemistry* **79**, 125524.

Nagasawa H., Suzuki T., Ito M. and Morioka M. (2001) Diffusion in single crystal of melilite: interdiffusion of Al + Al vs. Mg + Si. *Physics and Chemistry of Minerals* **28**, 706–710.

Norris T. L., Gancarz A. J., Rokop D. J. and Thomas K. W. (1983) Half-life of ^{26}Al. *Journal of Geophysical Research* **88**, B331–B333.

Park C., Wakaki S., Sakamoto N., Kobayashi S. and Yurimoto H. (2012) Oxygen isotopic variations of melilite crystals in a Type A CAI from Allende. *Meteoritics & Planetary Science* **47**, 2070−2083.

Park C., Nagashima K., Krot A. N., Huss G. R., Davis A. M. and Bizzarro M. (2017) Calcium-aluminum-rich inclusions with fractionation and unidentified nuclear effects (FUN CAIs): II. Heterogeneities of magnesium isotopes and ^{26}Al in the early Solar System inferred from in situ high-precision magnesium-isotope measurements. *Geochimica et Cosmochimica Acta* **201**, 6–24.

Podosek F. A., Zinner E. K., MacPherson G. J., Lundberg L. L. Brannon J. C. and Fahey

637 A. J. (1991) Correlated study of initial $^{87}Sr/^{86}Sr$ and Al-Mg isotopic systematics
638 and petrologic properties in a suite of refractory inclusions from the Allende
639 meteorite. *Geochimica et Cosmochimica Acta* **55**, 1083−1110.
640 Shewmon P. (1963) *Diffusion in Solids*, McGraw-Hill, New York.
641 Simon S. B., Davis A. M. and Grossman L. (1999) Origin of compact type A refractory
642 inclusions from CV3 carbonaceous chondrites. *Geochimica et Cosmochimica*
643 *Acta* **63**, 1233−1248.
644 Simon S. B. and Grossman L. (2004) A preferred method for the determination of bulk
645 compositions of coarse-grained refractory inclusions and some implications of the
646 results. *Geochimica et Cosmochimica Acta* **68**, 4237−4248.
647 Simon S. B., Grossman L. and Davis A. M. (2005) A unique type B inclusion from
648 Allende with evidence for multiple stages of melting. *Meteoritics & Planetary*
649 *Science* **40**, 461–475.
650 Stolper E. and Paque J. M. (1986) Crystallization sequences of Ca-Al-rich inclusions
651 from Allende: The effects of cooling rate and maximum temperature. *Geochimica*
652 *et Cosmochimica Acta* **50**, 1785–1806.
653 Wada S., Kawasaki N., Park C. and Yurimoto H. (2020) Melilite condensed from an ^{16}O-
654 poor gaseous reservoir: Evidence from a fine-grained Ca-Al-rich inclusion of
655 Northwest Africa 8613. *Geochimica et Cosmochimica Acta* **288**, 161–175.
656 Wakaki S., Itoh S., Tanaka T. and Yurimoto H. (2013) Petrology, trace element
657 abundances and oxygen isotopic compositions of a compound CAI-chondrule
658 object from Allende. *Geochimica et Cosmochimica Acta* **102**, 261–279.
659 Wark D. A. and Lovering J. F. (1982) The nature and origin of type B1 and B2 Ca-Al-rich
660 inclusions in the Allende meteorite. *Geochimica et Cosmochimica Acta* **46**, 2581–

2594.

Wark D. A. (1987) Plagioclase-rich inclusions in carbonaceous chondrite meteorites: liquid condensates? *Geochimica et Cosmochimica Acta* **51**, 221–242.

Wasserburg G. J., Lee T. and Papanastassiou D. A. (1977) Correlated O and Mg isotopic anomalies in Allende inclusions: II. Magnesium. *Geophysical Research Letters* **4**, 299–302.

Yamamoto D., Tachibana S., Kawasaki N., Kamibayashi M. and Yurimoto H. (2019) Oxygen isotope exchange between CAI melt and water vapor: An experimental study. (abstract #2157) 82nd Annual Meteoritical Society Meeting.

Yoshitake M., Koide Y. and Yurimoto H. (2005) Correlations between oxygen-isotopic composition and petrologic setting in a coarse-grained Ca, Al-rich inclusion. *Geochimica et Cosmochimica Acta* **69**, 2663–2674.

Yurimoto H., Nagasawa H., Mori Y. and Matsubaya O. (1994) Micro-distribution of oxygen isotopes in a refractory inclusion from the Allende meteorite. *Earth and Planetary Science Letters* **128**, 47–53.

Yurimoto H., Ito M. and Nagasawa H. (1998) Oxygen isotope exchange between refractory inclusion in Allende and solar nebula gas. *Science* **282**, 1874–1877.

Yurimoto H. and Wasson J. T. (2002) Extremely rapid cooling of a carbonaceous-chondrite chondrule containing very ^{16}O-rich olivine and a ^{26}Mg-excess. *Geochimica et Cosmochimica Acta* **66**, 4355–4363.

Yurimoto H., Nagashima K. and Kunihiro T. (2003) High precision isotope micro-imaging of materials. *Applied Surface Science* **203–204**, 793–797.

684 Table 1. Average O-isotopic compositions (‰) of spinel in the core of Golfball.

Occurrence	No. of analyses	$\delta^{17}O$	2σ	$\delta^{18}O$	2σ	$\Delta^{17}O$	2σ
Core, framboid	20	-47.9	1.9	-45.9	1.1	-24.1	1.8
Core, in fassaite	7	-48.1	2.0	-46.3	0.9	-24.1	1.9
Core, in lath melilite	8	-47.5	1.7	-45.8	1.1	-23.7	2.1
Average	**35**	**-47.9**	**1.9**	**-45.9**	**1.1**	**-24.0**	**1.9**

685 Bold data: average values of all measurements for spinel

686

687 Table 2. Mg-isotopic compositions (‰) and $^{27}Al/^{24}Mg$ ratios of minerals in the core of

688 Golfball.

Spot #	$^{27}Al/^{24}Mg$	2σ	$\delta^{26}Mg^*$	2σ	$\delta^{25}Mg$	2σ
Melilite, core, blocky, Al-rich grains						
5	16.1	0.1	4.9	1.3	1.0	1.1
6	20.4	0.1	7.2	1.3	0.2	1.0
8	16.6	0.1	5.3	1.3	1.1	1.0
9	24.3	0.1	7.4	1.2	1.7	1.1
183	23.7	0.6	6.9	1.7	1.4	1.5
184	24.0	0.4	7.7	1.2	0.3	1.4
185	25.1	0.4	8.2	1.2	1.2	1.4
187	27.4	0.4	9.4	1.2	1.7	1.4
189	20.3	0.3	6.2	1.2	1.8	1.4
191	42.2	1.1	13.3	1.2	2.2	1.5
192	25.9	0.6	7.5	1.3	2.7	1.4
193	17.0	0.2	5.0	1.1	1.9	1.4
Melilite, core, blocky, overgrown grains						
229	5.00	0.01	1.51	0.13	1.73	0.09
311	6.10	0.08	1.92	0.12	1.80	0.05
312	4.80	0.03	1.51	0.13	1.93	0.05
Spinel, core, framboid						
351	2.480	0.001	0.73	0.08	1.80	0.06
352	2.484	0.005	0.82	0.08	1.75	0.04
353	2.497	0.004	0.74	0.07	1.85	0.04
365	2.487	0.004	0.72	0.07	1.84	0.04
367	2.498	0.004	0.81	0.08	1.68	0.05
Spinel, core, in melilite						
347	2.484	0.006	0.73	0.07	1.82	0.03

689

690

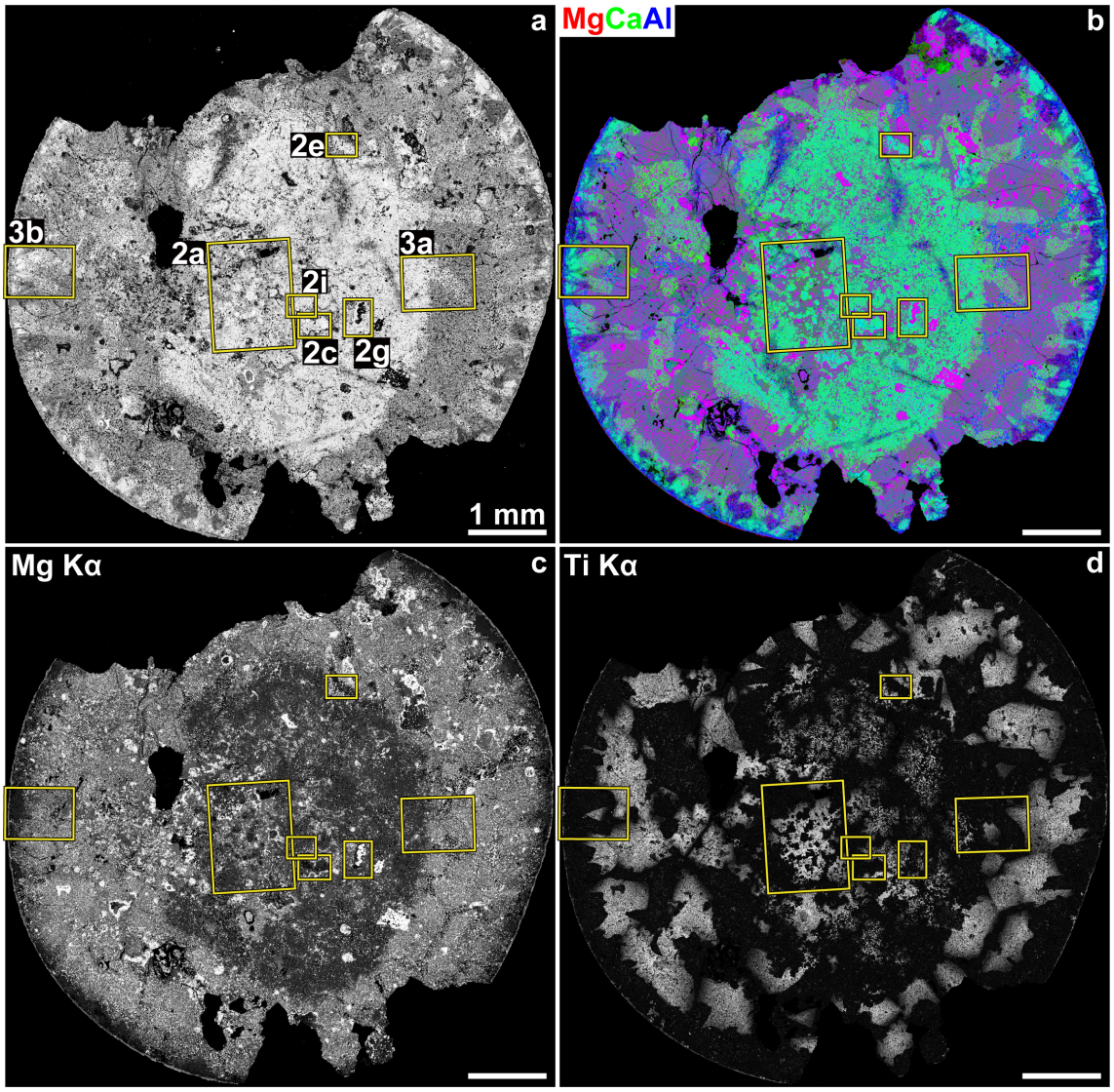

Figure 1. (a) Backscattered electron (BSE) image of an Allende Type B CAI Golfball, section GBL2. Yellow boxes indicate the areas shown in Figs. 2 and 3. (b) Combined X-ray elemental map with Mg (red), Ca (green), and Al (blue), (c) Mg Kα elemental map, and (d) Ti Kα elemental map of the same field of view. Melilite at the outermost edge of the inclusion appears white in (a) and blue in (b). The melilite core appears white in (a) and green in (b). The spinel-fassaite mantle is gray in (a) and purple in (b). Note melilite laths extending from the core into the mantle, visible in (a) and (b).

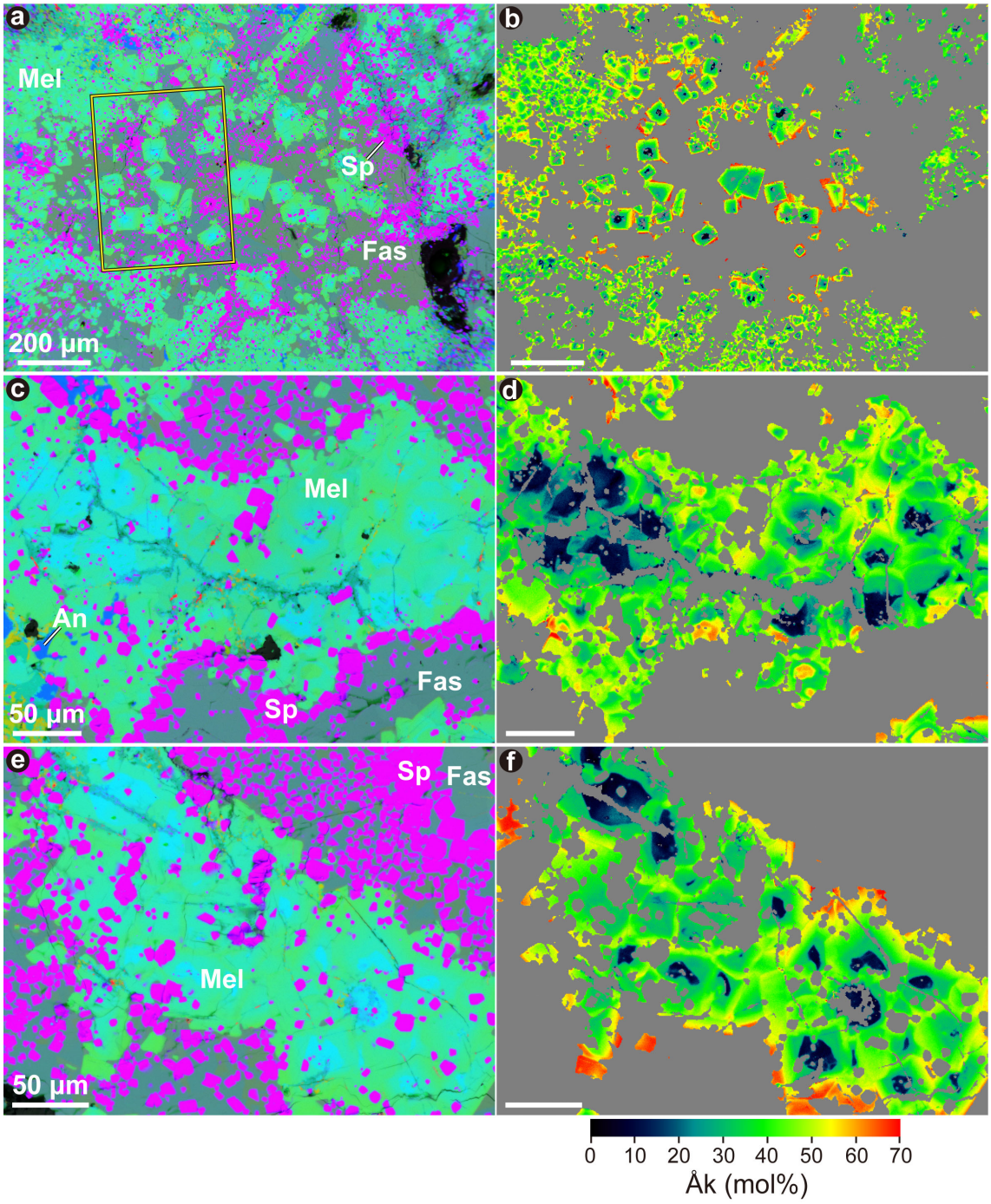

699

700 Figure 2. Combined X-ray elemental map of areas indicated in Fig. 1, showing Mg (red),
701 Ca (green), and Al (blue) and corresponding quantitative map of åkermanite content (Åk)
702 in melilite from the same areas. Mineral phases except melilite and cracks are masked in
703 gray. (a,b) area 1; (c,d) area 2; (e,f) area 3; (g,h) area 4; (i,j) area 5. Areas 1 and 4 are
704 rotated ~90 degrees from the view in Fig. 1. An, anorthite; Fas, fassaite; Mel, melilite; Sp,

spinel.

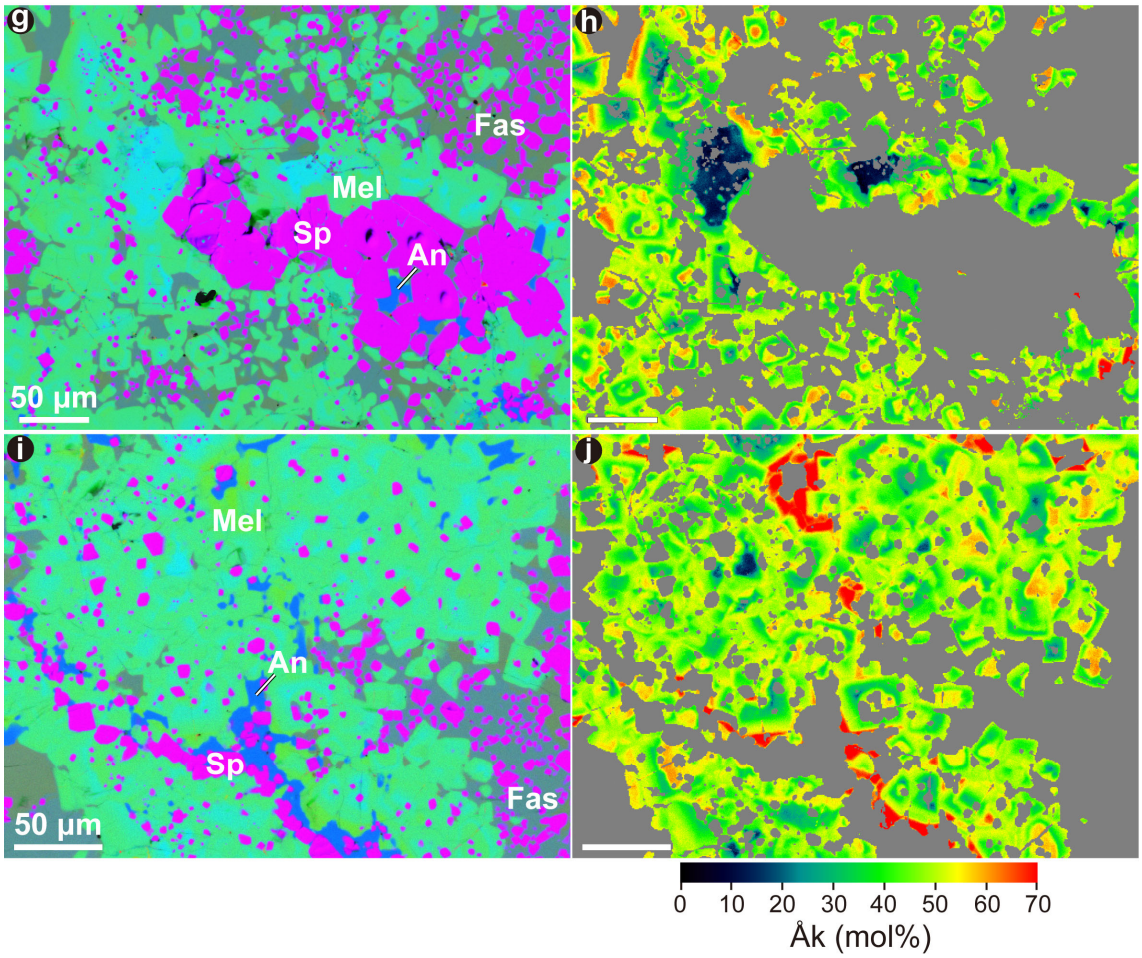

707

708 Figure 2 (*continued*)

709

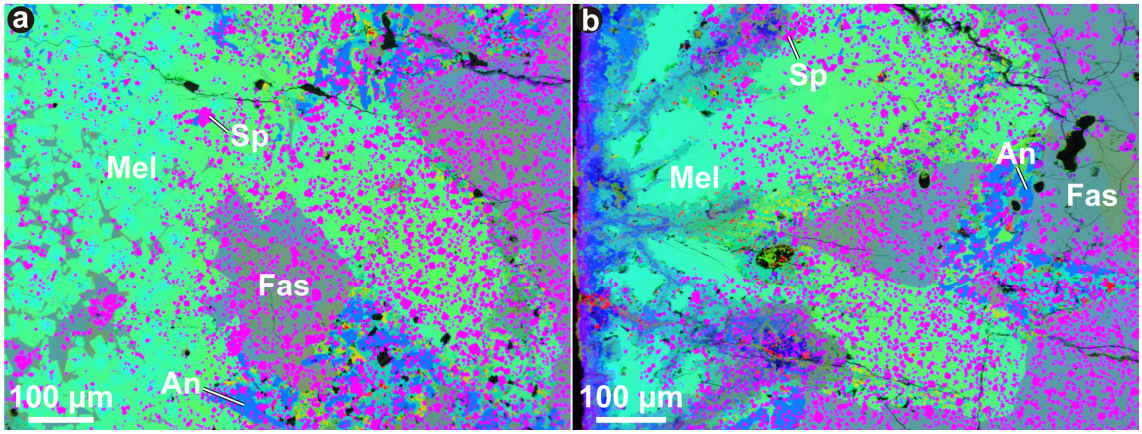

Figure 3. Combined X-ray elemental map of areas indicated in Fig. 1, showing Mg (red), Ca (green), and Al (blue). An, anorthite; Fas, fassaite; Mel, melilite; Sp, spinel. BSE images of the same areas are shown in Supplementary materials.

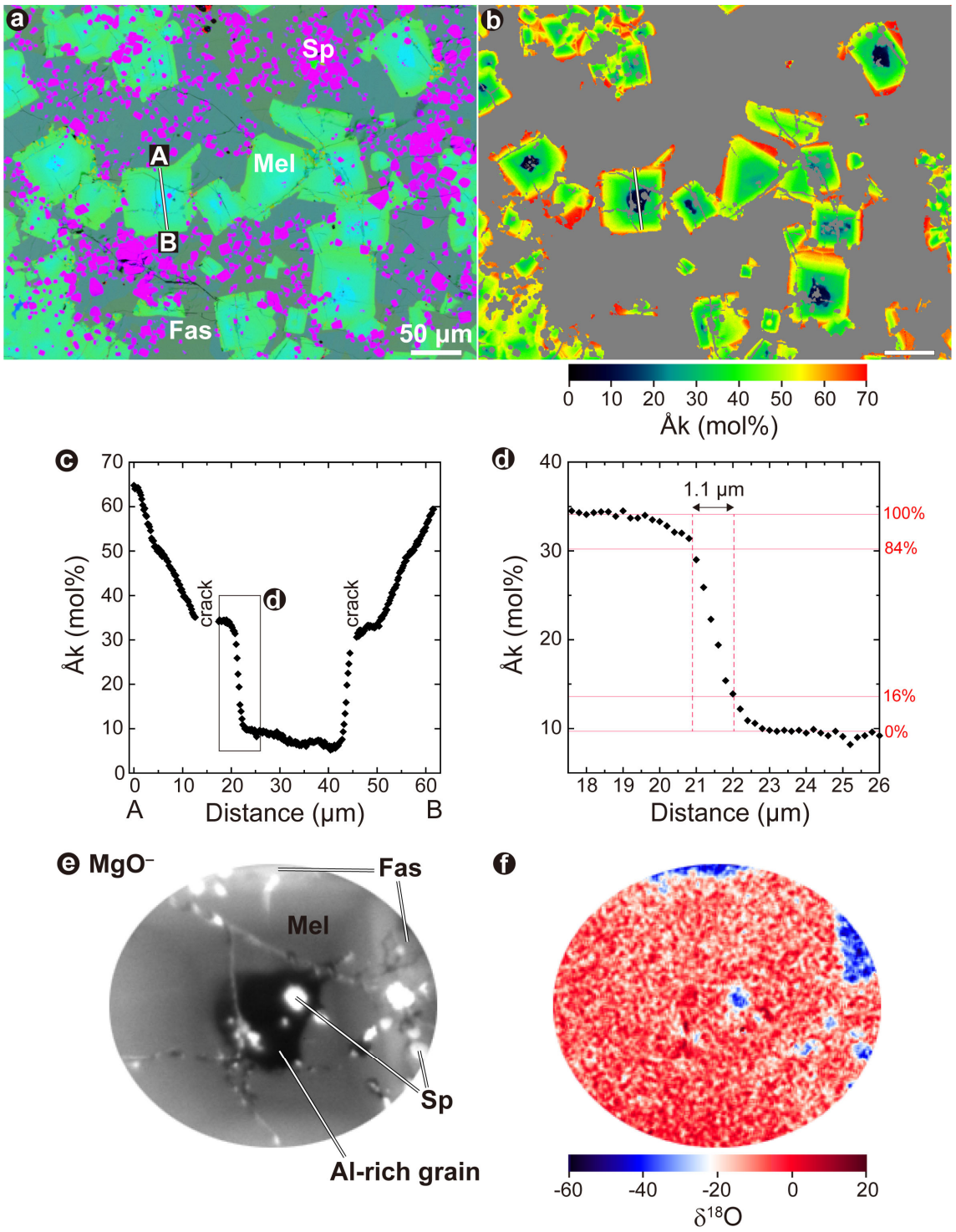

Figure 4. (a) Combined X-ray elemental map of an area indicated by yellow box in Fig. 2a, showing Mg (red), Ca (green), and Al (blue). (b) Quantitative map of åkermanite content (Åk) in melilite shown in (a). Mineral phases except melilite and cracks are

masked in gray. (c,d) Zoning of åkermanite content in melilite along the line A−B in (a). (e) MgO^- isotope image and (f) $\delta^{18}O$ quantitative isotope ratio image of the same melilite crystal examined in (c,d). An, anorthite; Fas, fassaite; Mel, melilite; Sp, spinel.

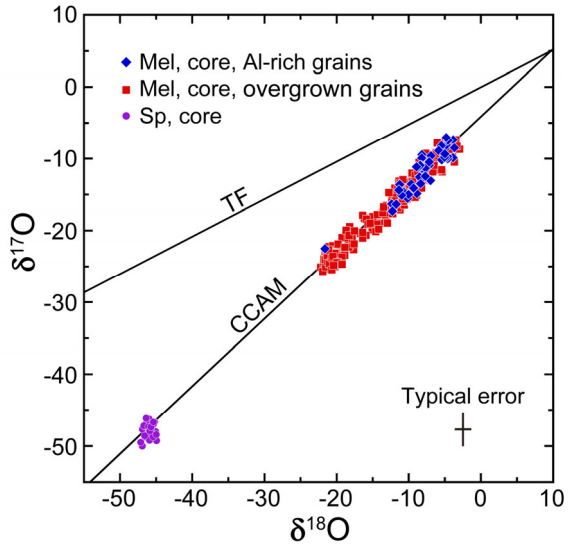

723

724 Figure 5. O-isotopic compositions of blocky melilite and spinel in Golfball. Plots of
725 "overgrown grains" (red squares) include melilite data across boundaries between Al-rich
726 and overgrown grains (Table S2). Typical error (2σ) is shown. TF, terrestrial fractionation
727 line; CCAM, carbonaceous chondrite anhydrous mineral line; Mel, melilite; Sp, spinel.

728

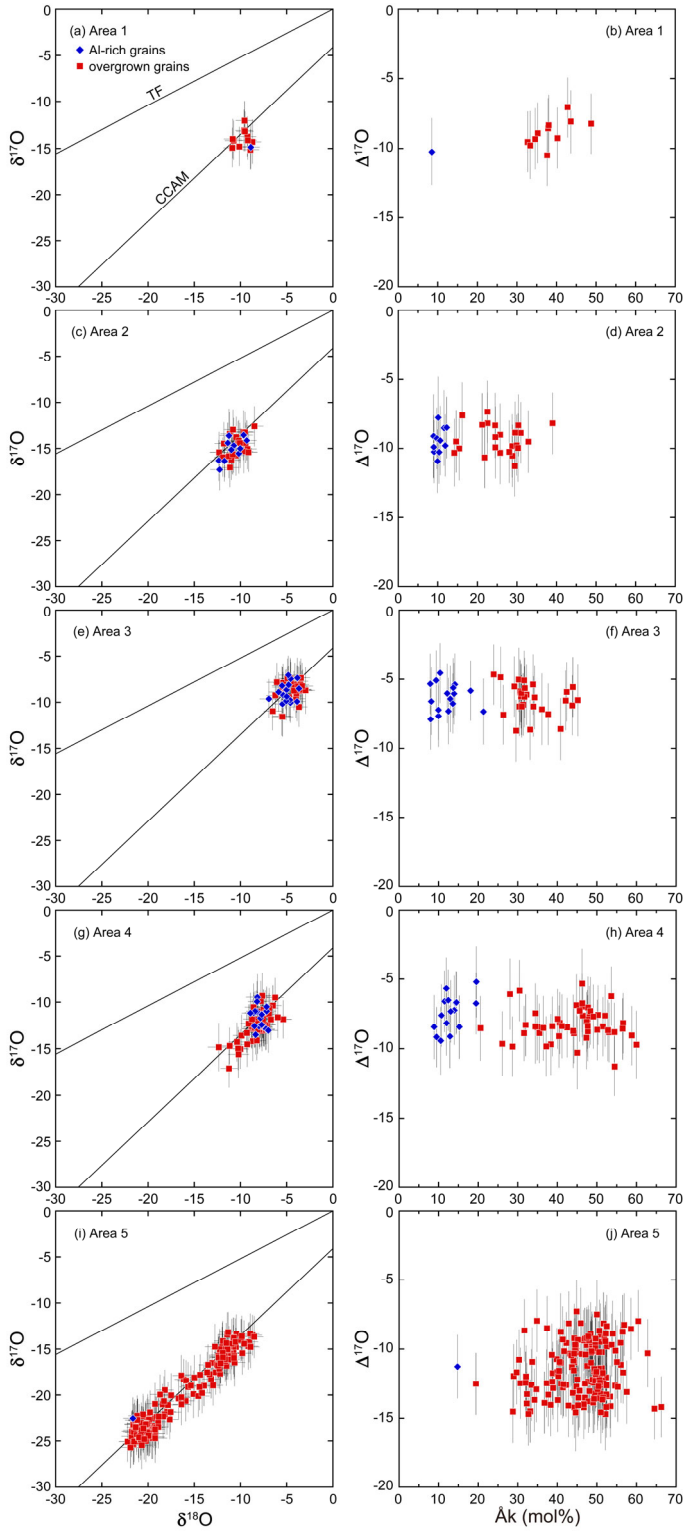

729

730 Figure 6. O-isotopic compositions and their relationships with åkermanite content (Åk)

731 of Al-rich and overgrown melilite grains in each area of the core. Errors correspond to 2σ.

732 TF, terrestrial fractionation line; CCAM, carbonaceous chondrite anhydrous mineral line.

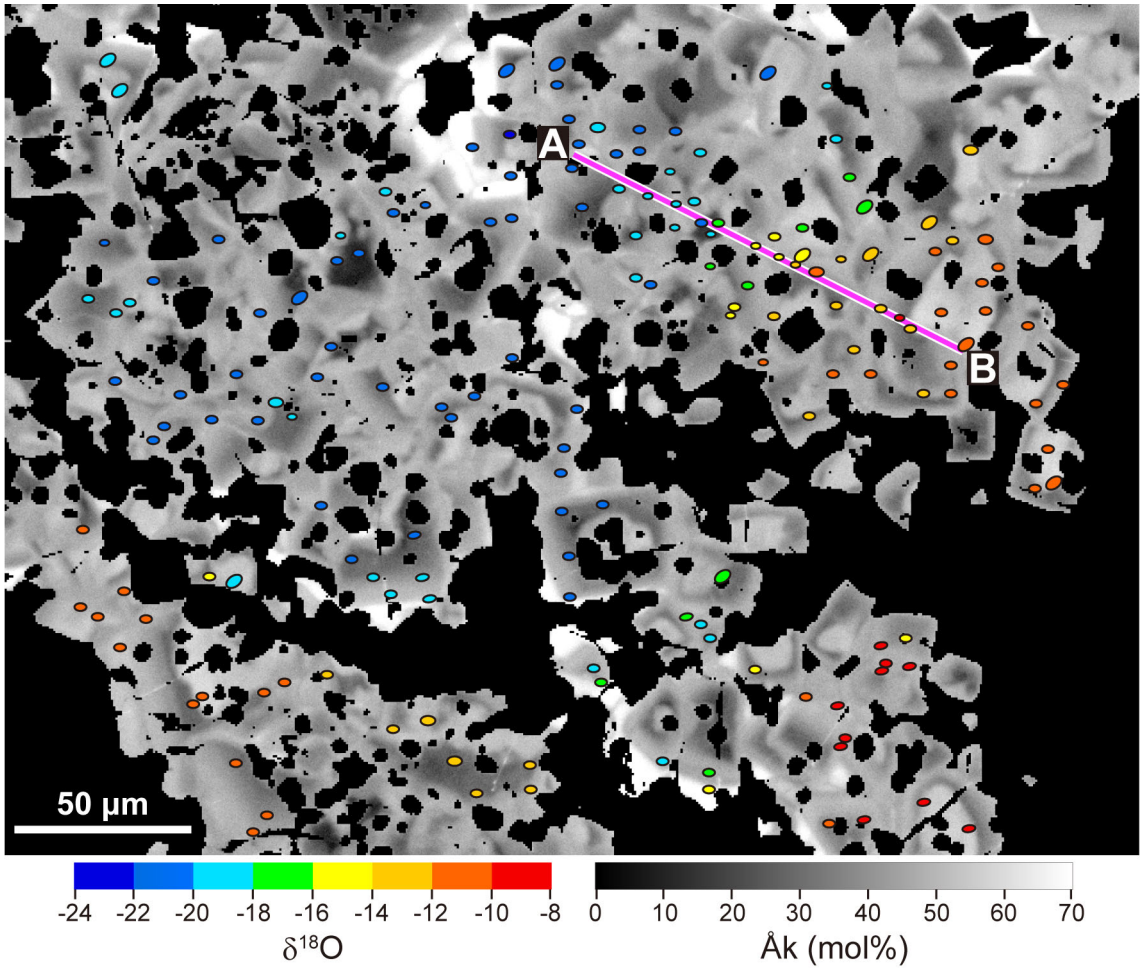

733

734 Figure 7. $\delta^{18}O$ variations of melilite crystals in area 5 overlaid on quantitative map of

735 åkermanite content (Åk). Mineral phases except melilite and cracks are masked in black.

736 Each circle corresponds to spot sizes of *in situ* O-isotope measurements. Data collected

737 along the A-B traverse are shown in Fig. 9.

738

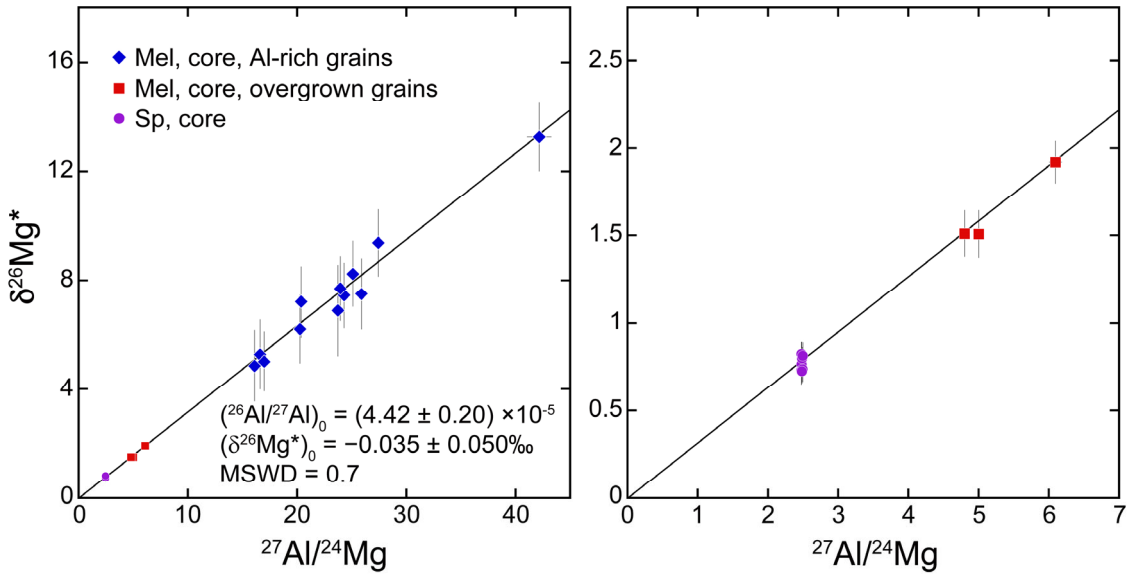

739

740 Figure 8. ^{26}Al–^{26}Mg evolution diagrams for minerals in the core of Golfball, each of
741 which shows different ranges of $^{27}Al/^{24}Mg$ ratio. Isoplot Model 1 (Ludwig, 2003) is used
742 to fit isochrons. Errors correspond to 2σ. Symbols without error bars exhibit errors smaller
743 than their symbol sizes. Mel, melilite; Sp, spinel.

744

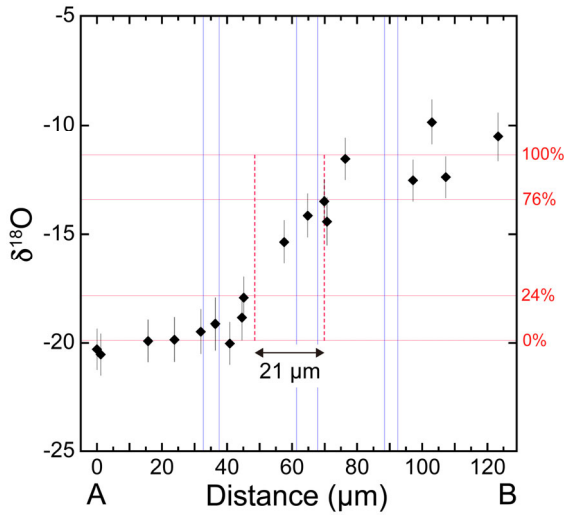

Figure 9. Variations of O-isotopic compositions ($\delta^{18}O$) along the line A−B in Fig. 7. Spot data within 4 μm distances from the line are used. Blue vertical lines correspond to positions of grain boundaries of melilite crystals. A diffusion distance, $2(Dt)^{1/2}$, under the initial condition of two semi-infinite sources is defined by the width between the 24% and 76% level (Shewmon, 1963). Errors correspond to 2σ. The spatial resolution of each point is 2−3 μm, determined by the probe size.

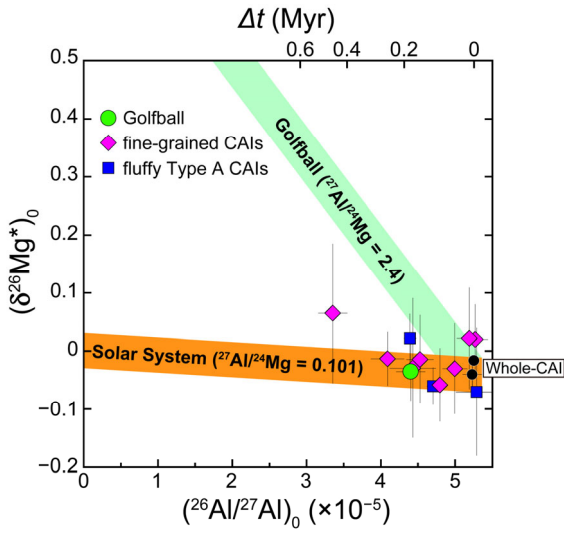

753

754 Figure 10. Mg-isotope evolution of Golfball. A calculated Mg-isotope evolution curve for
755 Golfball from whole-rock CAI $^{26}Al/^{27}Al$ and $\delta^{26}Mg^*$ values (black circles, Jacobsen et
756 al., 2008; Larsen et al., 2011) is shown as a green-colored area and that for a solar-
757 composition gas ($^{27}Al/^{24}Mg$ = 0.101) is shown as an orange-colored area. Colored
758 diamonds indicate initial $^{26}Al/^{27}Al$ and $\delta^{26}Mg^*$ values for fine-grained CAIs in CV
759 chondrites (MacPherson et al., 2010, 2012; Kawasaki et al., 2020; Wada et al., 2020) and
760 colored squares indicate those for fluffy Type A CAIs (MacPherson et al., 2012; Kawasaki
761 et al., 2019). The $^{27}Al/^{24}Mg$ ratio of the Solar System is obtained from Lodders (2003).
762 Errors correspond to 2σ.